Nano Research 2013, 6(2): 149–158
DOI 10.1007/s12274-013-0290-1
Research Article

ISSN 1998-0124
CN 11-5974/O4

Improved photoconductive properties of composite nanofibers based on aligned conjugated polymer and single-walled carbon nanotubes

Florian Massuyeau[1] (✉), Yuanchun Zhao[1], Abdel Aziz El Mel[1], Abu Yaya[1], Frédéric Geschier[1], Eric Gautron[1], Serge Lefrant[1], Jean Yves Mevellec[1], Chris Ewels[1], Chain-Shu Hsu[2], Eric Faulques[1], Jany Wéry[1], and Jean Luc Duvail[1] (✉)

[1] *Institut des Matériaux Jean Rouxel, UMR6502 CNRS, Université de Nantes, 2 rue de la Houssinière, F-44322 Nantes, France*

[2] *Department of Applied Chemistry, Chiao Tung University, 1001 Ta Hsueh Road, Hsin-Chu 30010, Taiwan, China*

Received: 3 October 2012
Revised: 13 December 2012
Accepted: 28 December 2012

KEYWORDS

Tubular nanocomposites, single-walled carbon nanotube (SWNT), photoconductivity, transport properties, conjugated polymer, density functional theory (DFT) calculation

ABSTRACT

We successfully address the challenge of aligning single-walled carbon nanotubes (SWNTs) and conjugated polymer chains in composite nanofibers for enhancing their opto-electrical properties. A pore-filling template strategy has been developed to prepare such nanocomposites from SWNTs and poly(para-phenylene vinylene) (PPV) chains, with both species well-oriented aligned along the pore axis. Addition of the SWNTs leads to a remarkable increase in photocurrent of four orders of magnitude as compared to equivalent pristine PPV nanofibers. Further analysis indicates that the strong photocurrent enhancement is not simply an effect of alignment, but additionally benefits from alignment-enhanced interaction of polymer chains with SWNTs, as supported by density functional theory (DFT) calculations.

1 Introduction

Organic semi-conductors have emerged as cost effective functional materials for organic electronic devices such as flexible displays and organic light emitting diodes (OLEDs), field effect transistors (FET), and photovoltaic cells (see Ref. [1] and references therein). In this field of research, a huge effort has been focused on nanocomposites combining conjugated polymer (CPs) with single-walled carbon nanotubes (SWNTs) [2] which possess intrinsic properties complementary to those of CPs, and in particular with

Address correspondence to Florian Massuyeau, florian.massuyeau@cnrs-imn.fr; Jean Luc Duvail, duvail@cnrs-imn.fr

poly(para-phenylene vinylene) (PPV) derivatives [3, 4]. Besides providing mechanical reinforcement of the polymer matrix [5], they can act as direct pathways for charge transport in OLEDs to enhance the electroluminescence efficiency [6], as well as exciton separators to improve the photoconduction of solar cells [7]. The high aspect ratio of SWNTs can greatly enhance the electrical, optical and thermal properties of a host composite. However in order to benefit from this effect at only small SWNT concentrations, SWNT alignment in the composite is generally required [8]. For example, high density arrays of nanofibers are now considered as a promising alternative to bulk heterojunction solar cell structures, by achieving optimal exciton dissociation and charge transport in organic photovoltaic cells [9, 10].

A key challenge is the design of composite CP–SWNT nanostructures with well-ordered carbon nanotubes and polymer chains. Carbon nanotube alignment has been achieved in composite films via melt pressing [11], spin-coating [12] or by applying an external electric [13] or magnetic field [14] during synthesis. Composite nanofibers have also been prepared by electrospinning [15] and template-directed electrochemical synthesis [16]. However, an alternative route resulting in ordered arrays of composite nanofibers with well defined diameters and lengths would be better suited for the applications mentioned above.

In this work, we show that both the conductive and photoconductive properties of composite PPV–SWNT nanofibers strongly benefit from well-aligned conjugated polymer chains and SWNTs induced by solvent-assisted wetting template synthesis in a porous alumina membrane. Preferential alignment of both SWNTs and PPV chains along the pore axis is demonstrated by polarized micro-Raman spectroscopy. Moreover, density functional theory (DFT) calculations show there is a strong thermodynamic driving force for PPV–SWNT interaction, with the axis of the polymer preferentially aligning with that of the SWNT. The photocurrent of the resulting composites nanofibers is a remarkable four orders of magnitude larger than that of equivalent nanotubular PPV. The excellent charge carrier behaviour of the SWNTs is fully exploited in the composite nanofibers due to the SWNT alignment. Additionally, further analysis of the current and photocurrent measurements coupled with transient photoluminescence studies, demonstrates that the large photocurrent increase also benefits from the alignment of the polymer chains with the SWNTs. We attribute this to enhanced dissociation of excitons at aligned polymer–SWNT interfaces.

This study provides important new insight for improving (photo)conductive properties of nanocomposites. The versatile strategy used to achieve arrays of well-aligned composite nanofibers containing well-oriented conjugated polymer chains and SWNTs suggests a promising route to prepare highly efficient photovoltaic devices.

2 Methods

2.1 Experimental details

The procedure to synthesize the composite nanofibers is presented in Scheme 1(a). The nanofibers are kept inside the pores of the anodized aluminium oxide (AAO) template for all the measurements, except for the studies by scanning electron microscopy (SEM) and some of the studies by transmission electron microscopy (TEM) where the AAO membrane was etched by immersion in NaOH solution for several hours. After this removal, the nanofibers were collected on a Si substrate and washed several times with distilled water.

A JEOL 7600F field emission scanning electron microscope (FE-SEM) was used. The photoluminescence spectra of individual SWNTs were measured by a RFS 100 Bruker FT Raman spectrometer using an excitation line at 1064 nm. For the polarized micro-Raman study, a Jobin Yvon T64000 spectrometer and a Krypton laser at 647.1 nm coupled to a microscope was used to reach a probe size of about 2 μm. The photoluminescence (PL) decays were acquired with a Hamamatsu C7700 streak camera coupled to an imaging spectrograph. The 400 nm excitation line was provided by a Spectra-Physics Hurricane X laser system (100 fs, 1 kHz). Photoconductivity measurements were performed on the whole cross-section of the membrane by using the 488 nm line of an argon laser. The experimental setup is shown in Scheme 1(b). Both sides of the AAO membranes impregnated with

PPV or composite PPV–SWNTs were coated with a gold thin layer obtained by evaporation and contacted to the external circuit with a silver paste. The samples were placed into an Oxford cryostat under helium atmosphere. The dark current and the photocurrent were measured with a Keithley digital electrometer model 6517A. The current densities have been calculated by considering a nanofiber density in AAO of 10^9 cm^{-2}, an external diameter of 250 nm and a nanofiber wall thickness of about 20 nm, as shown by SEM and TEM investigations.

TEM experiments were carried out on a cold field emission gun (CFEG) Hitachi HF 2000 microscope operating at 200 kV with a Scherzer resolution of 0.23 nm. The energy-dispersive X-ray spectra (EDX) on TEM were obtained by using a Kevex Super-Quantek Si–Li detector. For the TEM studies, osmium tetroxide staining was used because of its known specific reactivity with polymers containing double carbon bonds [17]. The impregnated membrane was first stained with osmium tetroxide vapours. Then the stained samples were embedded in a Spurr epoxy resin and a Reichert Jung Super Nova microtome equipped with a Drukker diamond knife was used to cut slices thinner than 100 nm. The slices were then deposited on a copper grid covered with a holey carbon thin film. TEM images are shown in Fig. S1 in the Electronic Supplementary Material (ESM).

2.2 Calculations

Density functional calculations [18, 19] used the local density approximation with 2 × 2 × 1 k-point grid for graphene and a 1 × 1 × 2 k-point grid for the nanotubes. A localized Gaussian basis set with 22 functions per carbon and 12 per hydrogen were used, with Hartwigsen, Goedecker and Hütter relativistic pseudopotentials. A Fermi temperature smearing for the electron population of kT = 0.04 eV was incorporated to improve the convergence. Hexagonal supercells were used containing nanotubes with lengths in the range 24.29–25.41 Å (160–400 atoms), to which we added distyrylbenzene (DSB), which serves as a model PPV oligomer. The graphene was modeled using a 8 × 8 graphene supercell (C_{128}). A large vacuum spacing was used in each case (at least 13.5 Å between tubes) to ensure no inter-system interaction. Isolated tubes and graphene were fully relaxed and then held fixed once the DSB was added. The DSB was then fully geometrically optimized. Binding energies were calculated in comparison to the isolated separate components, i.e., $E_B = E_{CNT–DSB} – (E_{CNT} + E_{DSB})$. Inter–DSB interaction was calculated with two DSB chains in a large hexagonal supercell with full atomic relaxation of both chains.

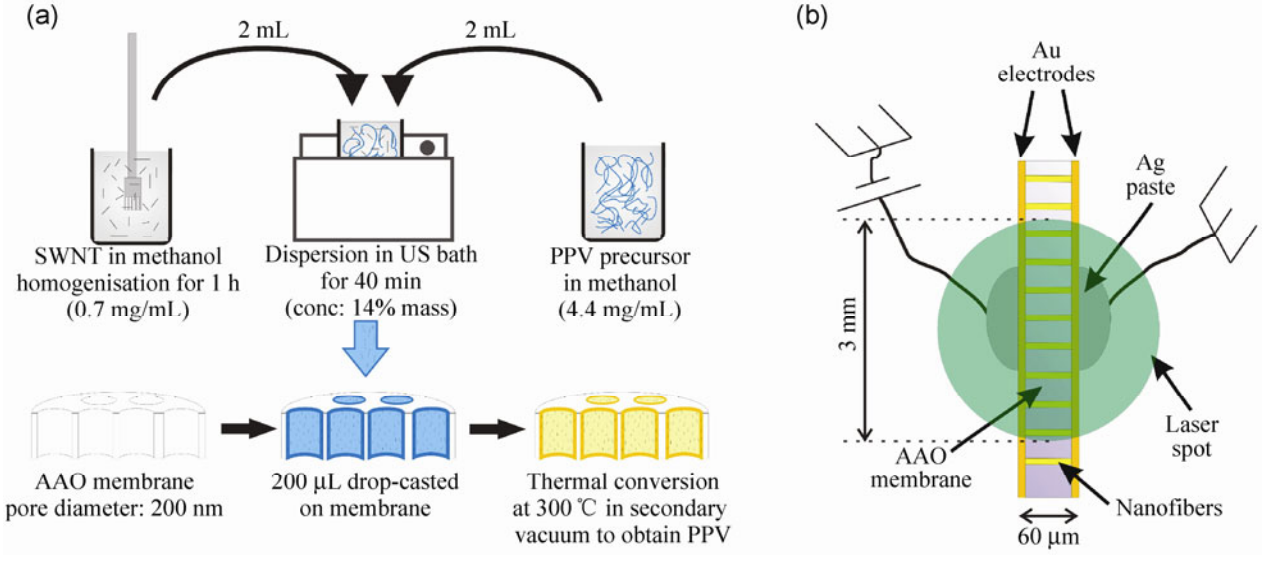

Scheme 1 (a) Template synthesis procedure to fabricate the composite PPV–SWNT nanofibers. (b) Experimental set-up for the (photo)conductive measurements.

3 Results and discussion

The composite PPV–SWNT nanofibers were synthesized by dropping ~200 μL of an homogeneous solution containing both the SWNTs and the PPV precursor onto a commercial AAO nanoporous membrane with a nominal pore diameter of 200 nm. A similar process was used previously to fabricate pristine PPV nanofibers [20, 21]. The PPV precursor, poly(*p*-xylene tetrahydrothiophenium chloride) (PXT), was synthesized in our laboratory via a standard route [22]. SWNTs (metallic and semiconducting) 1–2 nm in diameter and 0.5–2 μm in length were purchased by Aldrich. The dispersion of the SWNT bundles was obtained first by an homogenisation treatment in methanol prior to mixing and sonication with the PXT polymer solution in methanol [23]. In the current study the weight ratio of SWNT:PXT was 14 wt.%. The SWNTs were well dispersed, as confirmed by the near-infrared (near-IR) emission spectrum of the resultant solution. Photoluminescence bands attributed to radiative recombination of the S_{11} singlet excitonic states of the SWNTs can be seen (see Fig. S2 in the ESM). These bands are located at 0.96 eV, 0.98 eV, 1.03 eV, and 1.08 eV and assigned respectively to (8,7), (11,1), (11,3), and (9,2) SWNTs, following Bachilo et al. [24]. Such bands are only observed when the SWNTs are well separated since non-radiative quenching occurs in bundles. Good SWNT dispersion is critical both for the penetration of SWNTs into nanopores and for fully benefiting from the unique features of SWNTs for the (photo)conduction. After methanol evaporation, the impregnated membranes were heated at 300 °C under dynamic secondary pumping (10^{-6} Torr) to fully convert the precursor into PPV.

The as-prepared samples were immersed in a 1 M NaOH solution for 30 min to remove the AAO template. Figures 1(a) and 1(b) show typical SEM images of composite nanofibers at different magnifications. Tubes are on average 60 μm long and 250 nm in diameter. The fibers can be partially torn or even disrupted due to their hollow core which can be clearly distinguished by both SEM and TEM, with a wall thickness in the range 20–30 nm (see the ESM). Chemical analysis by EDX of the composite nanofibers array (not shown here) confirms that these nanostructures are almost pure carbon with remaining traces of sodium and oxygen from the membrane dissolution. The inset in Fig. 1(c) shows a TEM image of the composite nanofibers on a copper grid, while the magnified main image shows two isolated SWNTs embedded in the tubule wall. The presence of SWNTs throughout the nanofibers is confirmed by Raman spectroscopy (Fig. 2).

We used a micro-Raman set-up (objective × 100) with an excitation line at 647.1 nm to draw a profile analysis along a cross-section of the AAO-membrane. The PPV precursor was not converted at this stage to prevent PPV luminescence, which masks the SWNT Raman signal. The radial breathing modes (RBMs) of SWNTs in the low frequency range are shown in Fig. 2. The SEM image inset indicates the corresponding areas (labelled from 1 to 7) where Raman spectra were recorded, area 1 being closest to the surface of

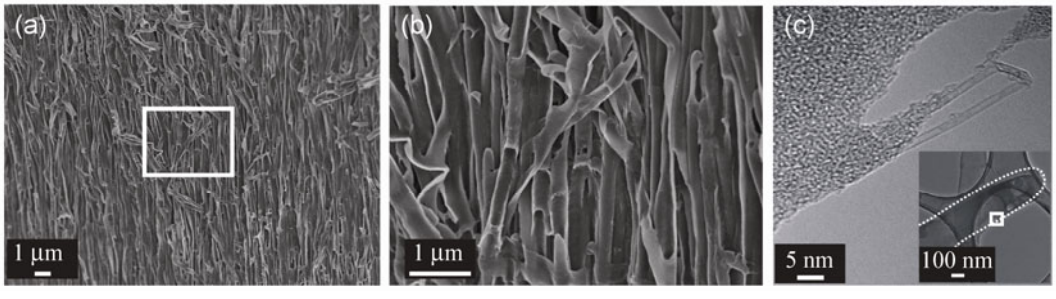

Figure 1 (a) Scanning electron microscopy (SEM) image of the composite nanofiber array after complete AAO removal (cross-section). (b) Magnified view of the white rectangular area in (a). (c) Transmission electron microscopy (TEM) zoom of the edge of a composite nanofiber showing the presence of both PPV and SWNTs (inset: Low magnification view showing the composite nanofiber delimited with white dotted line).

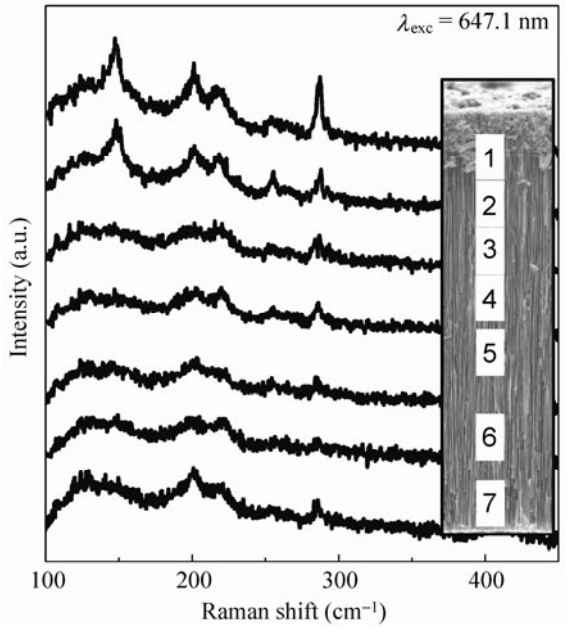

Figure 2 Raman spectra of PPV precursor–SWNT composite nanofibers measured along a AAO membrane cross-section. Insert SEM image shows the location of the analyzed area along the membrane cross-section (excitation wavelength at 647.1 nm).

impregnation. RBM modes are clearly seen in all the spectra, showing successful impregnation of SWNTs throughout the entire pore length (60 μm) of the AAO membrane. The progressive decrease in band intensity suggests a concentration gradient of SWNTs along the nanofibers.

Raman experiments with polarized light were performed on a cross-section of the impregnated AAO membrane to investigate the orientation of the SWNTs (Fig. 3). A 100 × microscope objective was used to both focus the 647.1 nm excitation line on the nanofibers and collect the resultant scattered light. The sample was mounted on a rotating stage which allows spectra to be recorded at variable angles θ_m between the direction of light polarization and the pore axes. Once again this study was performed prior to PPV thermal conversion to prevent the strong PPV Raman signal in the range of the SWNT G-band, i.e., 1,550–1,600 cm^{-1}. Raman spectra (Fig. 3(a)) of the RBM and the tangential G band modes were recorded with parallel polarization of the incoming and scattered light (VV configuration) as a function of the measured angle θ_m (Fig. 3(b)). For both modes, the Raman peak intensities decrease as θ_m varies from 0° to 90° and increase as θ_m varies from 90° to 180°. The G band intensity is shown in blue in a polar diagram (Fig. 3(c)) from θ_m = 0° to 360°. Strong optical anisotropy of the G band intensity is observed with a ratio I_{max}/I_{min} of ~5.6. Previous polarized Raman studies of isolated SWNTs showed that the G band intensity exhibits a

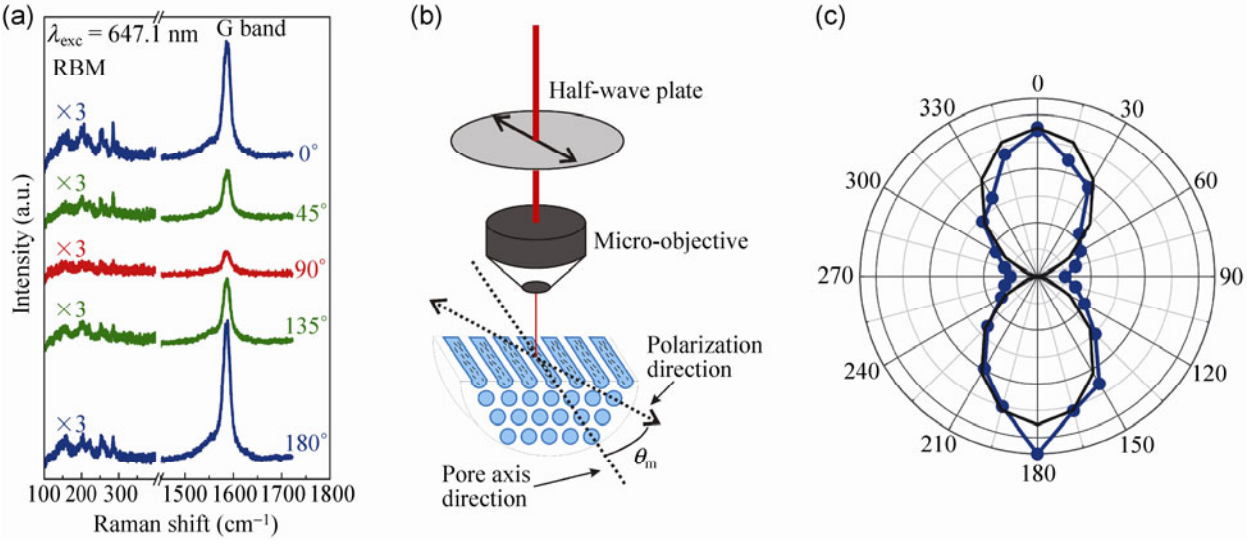

Figure 3 (a) Polarized Raman spectra in the VV configuration (see text) as a function of the measured angle θ_m between the laser polarization direction and the pore axis (excitation wavelength: 647.1 nm); the spectra were taken at cross-section location labeled 2 in Fig. 2. (b) Schematic view of the experimental setup. (c) Polar diagram showing the G band intensity of SWNTs as a function of θ_m. Experimental points are represented in blue (with lines as a guide to the eye), and the black line is the calculated $\cos^2\theta_m$ function normalized to the intensity at θ_m = 0°.

strong angular dependence which can be described by $I(\theta_m) \alpha \cos^2(\theta_m)$ [25–27], similar to that observed here. The RBM intensities also exhibit strong anisotropy (Fig. 3(a)), in agreement with previous work by Duesberg et al. [25]. Notice that these polarization properties have also been observed in the photoluminescence emission and absorption of aligned SWNTs [28]. The Raman signal reaches a maximum when the electric field direction (polarization direction) is parallel to the SWNT axis. Here, we observe this maximum for a polarization direction parallel to the pore axis, showing that the SWNTs are well oriented parallel to the pore and to the composite nanofiber axis.

A similar polarized Raman study after the PPV conversion inside the AAO membrane allows investigation of the polymer chain orientation within the composite nanofibers (see Fig. S3 in the ESM). Raman signal anisotropy has been previously used in this way to probe the intrinsic anisotropy of conjugated polymer chains [29]. The Raman spectrum of PPV is well known [30] and contains five main bands at 1,175, 1,330, 1,550, 1,586, and 1,625 cm^{-1}. In the present study, we focus on the three bands at 1,545, 1,581, and 1,624 cm^{-1} attributed to a mixing of stretching and bending of carbon bonds in the PPV backbone [23, 31]. The intensity of these three bands significantly decreases from $\theta_m = 0°$ to 90° and increases from $\theta_m = 90°$ to 180°, as for the Raman modes of the SWNTs. This angular dependence clearly demonstrates the PPV chains are strongly oriented with their backbone parallel to the composite nanofiber axis, similarly to the SWNTs.

The alignment can be partly attributed to the filtration process, which occurs through the nanopores of the AAO membrane. The presence of SWNTs throughout the nanofibers indicates that at the early stage of the filtration the PXT–SWNT material easily passes through the pores before the dispersion—slowly, but continuously—settles down and blocks any further pass-through. This effect could explain the strong concentration gradient along the AAO pore length as well as SWNTs accumulated at the surface on the wetting side. Another contribution to the alignment and the preferential orientation of the carbon nanotubes as well as polymer chains inside the pores is likely to come from the capillary forces. Indeed, the wetting and the drying of the solution within each nanochannel may act as driving forces to brush SWNTs and polymer chains along the pore axis [32, 33]. Otherwise polymer chains would tend to randomly self-assemble into aggregates and SWNTs could be significantly bent. Improvement of the impregnation technique is still needed in order to obtain more homogeneous composite nanofibers along the AAO membrane. In order to investigate whether polymer–SWNT interaction can further enhance this strong alignment we need to turn to DFT calculations. It can be noted that modelling of the interaction between SWNTs and PPV derivatives has already been achieved for PPV derivatives [34].

For the DFT calculations we used the DSB unit ($C_{22}H_{18}$) as a three-ring PPV oligomer. A binding energy of 0.62 eV was found for two parallel overlaid DSB chains. We then optimized the DSB chain geometry in various orientations neighboring multiple different metallic and semiconducting nanotubes, as well as a reference graphene sheet. The resultant structures for DSB neighboring a (6,6) nanotube are given in Fig. 4 and the binding energies are plotted in Fig. 5. In all cases, the DSB–SWNT binding energy is significantly stronger than that of DSB–DSB, showing that there will be strong and preferable binding between SWNTs and DSB. The most stable orientation is always with the DSB parallel to the nanotube axis, lying flat on the tube surface at a distance of about 3.1 Å. The DSB chain remains relatively flat, with small displacements

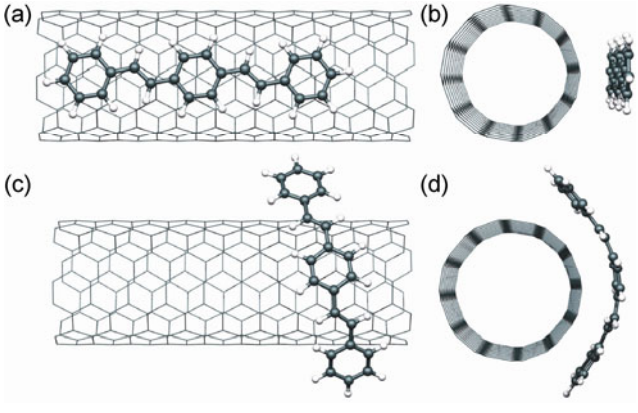

Figure 4 DFT optimized structures showing distyrylbenzene interacting with an infinite (6,6) metallic nanotube, (a), (b) parallel and (c), (d) perpendicular to the nanotube axis. (a), (c) show side and (b), (d) end views (showing the complete supercell).

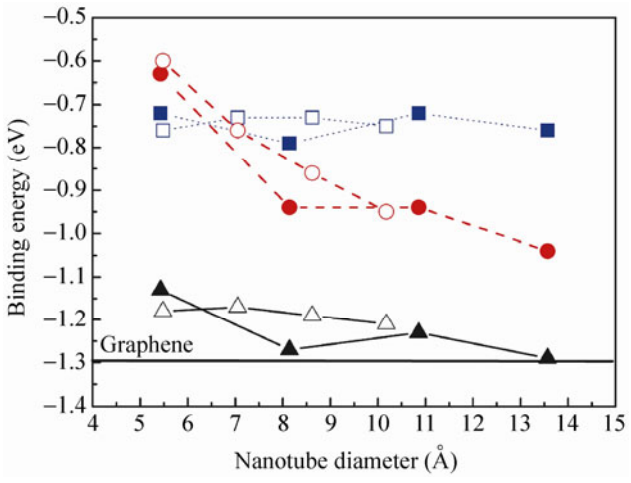

Figure 5 Calculated binding energy of distyrylbenzene to different SWNTs (eV). Empty symbols indicate semiconducting tubes, filled symbols indicate metallic ones. Triangles with a solid line (resp. squares with a dotted line) indicate DSB aligned along tube axis parallel (resp. perpendicular) to the nanotube surface; circles with a dashed line indicate DSB wrapped circumferentially around the nanotube, parallel to the nanotube surface. Metallic tubes are (4,4), (6,6), (8,8), and (10,10), semiconducting tubes are (7,0), (9,0), (11,0), and (13,0). DSB binding to graphene is given for comparison.

of the hydrogen atoms. There is no significant difference in binding energy between metallic and semiconducting tubes and instead, a weak binding dependence is observed on tube diameter favoring larger tubes (see the ESM. for numerical values). These results are consistent with previous literature calculations for other polymer–SWNT interactions [35, 36], which find either axial [35] or helical [36, 37] polymer alignment on the SWNT surface as a function of polymer backbone stiffness and side group type.

Placing the DSB along the axis but perpendicular to the SWNT wall (geometry not shown in Fig. 4), or curving the DSB chain circumferentially around the SWNT resulted in weaker binding (around 0.4 eV less), although still significant and still stronger than the DSB–DSB interactions. In a circumferential orientation, DSB curves in order to maximize π–π stacking interaction with the tube, and it is for this reason the energy difference between the circumferential and axial configurations decreases with increasing tube diameter (dashed lines, Fig. 5). No significant charge transfer between DSB and the SWNT was found in any of the calculations, but note that these are ground state calculations and do not reflect electron distribution after photon absorption and exciton formation. In summary, the calculations show there is a strong thermodynamic driving force for DSB–SWNT interaction, with the axis of the oligomer preferentially aligning with that of the nanotube.

The benefits of the strong preferential alignment of polymer chains and SWNTs, in terms of the conductivity and photoconductivity of the nanofibers, have been determined. The photocurrent (i.e., the additional contribution to the current due to illumination) in PPV nanofibers and composite PPV–SWNT nanofibers was measured for three samples of each type (Fig. 6(a)). The corresponding photocurrent densities, respectively $J_{PC}^{PPV\text{-}NF}$ and $J_{PC}^{Comp\ PPV-NF}$, were calculated. An excitation wavelength (λ_{exc} = 488 nm) and a bias electric field of 3330 V/cm were applied at different laser powers up to 100 mW. The photocurrent follows a power law as a function of the relative laser power, with an exponent value ranging between 0.8 and 0.9, in agreement with previous studies [38]. For the composite nanofibers, a remarkable increase in the photocurrent of up to four orders of magnitude is seen, independent of the laser power. This photocurrent enhancement due to the SWNTs in the host conjugated polymer is around two to three orders of magnitude greater than the ones previously measured in different SWNT–polymer nanocomposite films [39, 40]. A semi-quantitative analysis derived from a comparison of the conduction and the photoconduction with the case of nanocomposites films (see the ESM) confirms that the real photocurrent in the composite nanofibers is certainly enhanced by a factor significantly larger than 150. Percolation effects due to SWNTs have been shown to occur in composite films with a loading of around 2 wt.% thus improving their conductivity. Here, it is not possible to identify whether the SWNT network percolates, but it is clear that the alignment of SWNTs significantly contributes to the increase of the dark current conductivity, as SWNTs are efficient conduction pathways in comparison to undoped PPV. Furthermore, the analysis of the photoconduction measurements (see the ESM) strongly suggests that there exists an additional effect which accounts for the whole enhancement of photoconductivity. We propose that it can be attributed to the enhanced separation of excitons into free carriers

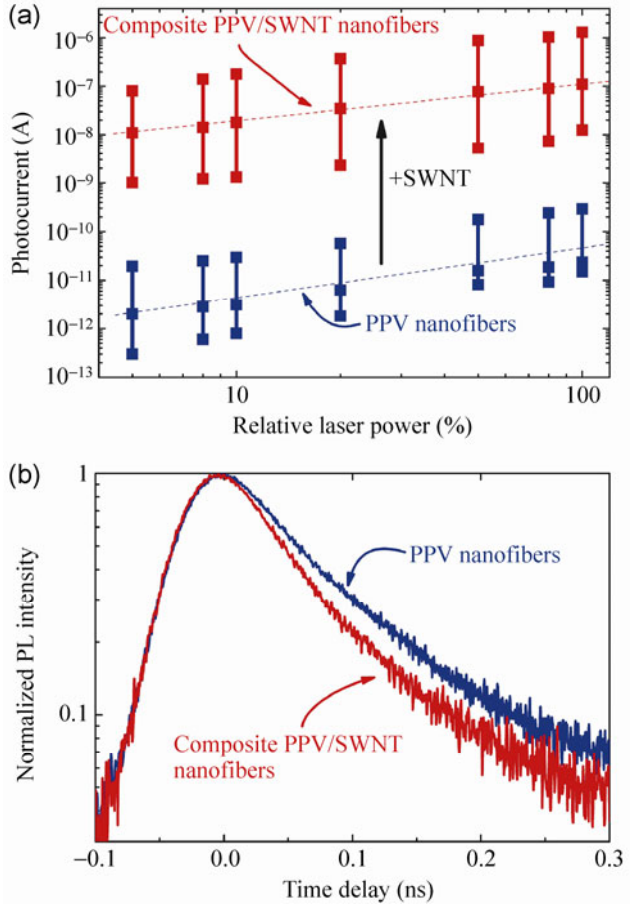

Figure 6 (a) Laser power dependence of the photocurrent at room temperature for PPV and composite PPV–SWNT nanofibers (three samples each; excitation at 488 nm). (b) PL delay dynamics of PPV and composite PPV–SWNT nanofibers inside AAO membrane, excitation wavelength: 400 nm.

due to the alignment of both the SWNTs and the polymer chains along the composite nanofiber axis, in comparison to that for randomly oriented SWNTs in nanocomposite films. To test this hypothesis, the charge separation was evaluated from a study of the transient photoluminescence (Fig. 6(b)). The lifetime decreased from 67 ps for PPV nanofibers to 55 ps for composite nanofibers. In pristine PPV at this excitation wavelength, excitons are preferentially created on short conjugated segments. The excitons then migrate from shorter to longer conjugated segments before radiative recombination occurs [41]. In the composite nanofibers, and as previously shown in conjugated polymer–SWNT composite films [42], the SWNT network efficiently separates the carriers during this migration. Thus, the non-radiative pathway becomes effective, resulting in the decrease of the PL lifetime but to an increase of the photocurrent. This huge enhancement of the photocurrent could strongly benefit the efficiency of optoelectronics devices such as photovoltaic cells and sensors.

4 Conclusion

Composite conjugated polymer–SWNT nanofibers have been produced for the first time by means of a wetting template method. The nano-confinement produces a strong alignment of SWNTs and polymer chains parallel to the pore axis, as confirmed by polarized micro-Raman spectroscopy. DFT calculations demonstrate that PPV chains stack preferentially parallel to the SWNT axis. The dissociation of excitons in charge carriers onto SWNTs observed by time-resolved photoluminescence, enhances the photocurrent by four orders of magnitude. The increase of the photoconductivity due to the alignment has been estimated to reach a factor of 150. This study shows the great potential of oriented SWNT–conducting polymer nanofibers, for example in ordered arrays for organic photovoltaic cells, for batteries and supercapacitors, or as individual nanofibers for sensors. Moreover, the simple and original nanostructuration strategy developed in this work can easily be used for any composite system available in solution. Thus, it opens a promising route to better understand the effect of SWNT–polymer alignment on the (photo)conductive properties of such hybrid systems.

Acknowledgements

We thank O. Chauvet for useful discussions and N. Stephant for useful help in SEM characterization. Part of this work was funded by the French National Research Agency (ANR) programme No. ANR-08-BLAN-0180-CSD3 entitled “Nanormade”.

Electronic Supplementary Material: Supplementary material (details of numerical methods, TEM images of composite nanofibers with EDX analysis, IR emission spectra of composite solution precursor PXT/SWNT before and after dispersion of SWNTs, binding energies (eV) of DSB on different carbon nanotubes and different

arrangements and variation of binding energies with diameter) is available in the online version of this article at http://dx.doi.org/10.1007/s12274-013-0290-1.

References

[1] Nalwa, H. S. *Handbook of Organic Electronics and Photonics*; American Scientific Publishers: Valencia, 2008.

[2] Harris, P. J. F. Carbon nanotube composites. *Int. Mater. Rev.* **2004**, *49*, 31–43.

[3] Dalton, A. B.; Stephan, C.; Coleman, J. N.; McCarthy, B.; Ajayan, P. M.; Lefrant, S.; Bernier, P.; Blau, W. J.; Byrne, H. J. Selective interaction of a semiconjugated organic polymer with single-wall nanotubes. *J. Phys. Chem. B* **2000**, *104*, 10012–10016.

[4] Steuerman, D. W.; Star, A.; Narizzano, R.; Choi, H.; Ries, R. S.; Nicolini, C.; Stoddart, J. F.; Heath, J. R. Interactions between conjugated polymers and single-walled carbon nanotubes. *J. Phys. Chem. B* **2002**, *106*, 3124–3130.

[5] Cadek, M.; Coleman, J. N.; Ryan, K. P.; Nicolosi, V.; Bister, G.; Fonseca, A.; Nagy, J. B.; Szostak, K.; Beguin, F.; Blau, W. J. Reinforcement of polymers with carbon nanotubes: The role of nanotube surface area. *Nano Lett.* **2004**, *4*, 353–356.

[6] Woo, H. S.; Czerw, R.; Webster, S.; Carroll, D. L.; Ballato, J.; Strevens, A. E.; O'Brien, D.; Blau, W. J. Hole blocking in carbon nanotube–polymer composite organic light-emitting diodes based on poly (m-phenylene vinylene-co-2,5-dioctoxy-p-phenylene vinylene). *Appl. Phys. Lett.* **2000**, *77*, 1393–1395.

[7] Hoppe, H.; Sariciftci, N. S. Polymer solar cells. *Adv. Polym. Sci.* **2008**, *214*, 1–86.

[8] Murakami, Y.; Chiashi, S.; Miyauchi, Y.; Hu, M. H.; Ogura, M.; Okubo, T.; Maruyama, S. Growth of vertically aligned single-walled carbon nanotube films on quartz substrates and their optical anisotropy. *Chem. Phys. Lett.* **2004**, *385*, 298–303.

[9] Yang, X.; Loos, J. Toward high-performance polymer solar cells: The importance of morphology control. *Macromolecules* **2007**, *40*, 1353–1362.

[10] Xin, H.; Reid, O. G.; Ren, G. Q.; Kim, F. S.; Ginger, D. S.; Jenekhe, S. A. Polymer nanowire/fullerene bulk heterojunction solar cells: How nanostructure determines photovoltaic properties. *ACS Nano* **2010**, *4*, 1861–1872.

[11] Thostenson, E. T.; Chou, T. W. Aligned multi-walled carbon nanotube-reinforced composites: Processing and mechanical characterization. *J. Phys. D Appl. Phys.* **2002**, *35*, L77–L80.

[12] Safadi, B.; Andrews, R.; Grulke, E. A. Multiwalled carbon nanotube polymer composites: Synthesis and characterization of thin films. *J. Appl. Polym. Sci.* **2002**, *84*, 2660–2669.

[13] Zhang, Y. G.; Chang, A. L.; Cao, J.; Wang, Q.; Kim, W.; Li, Y. M.; Morris, N.; Yenilmez, E.; Kong, J.; Dai, H. J. Electric-field-directed growth of aligned single-walled carbon nanotubes. *Appl. Phys. Lett.* **2001**, *79*, 3155–3157.

[14] Kimura, T.; Ago, H.; Tobita, M.; Ohshima, S.; Kyotani, M.; Yumura, M. Polymer composites of carbon nanotubes aligned by a magnetic field. *Adv. Mater.* **2002**, *14*, 1380–1383.

[15] Ko, F.; Gogotsi, Y.; Ali, A.; Naguib, N.; Ye, H. H.; Yang, G. L.; Li, C.; Willis, P. Electrospinning of continuous carbon nanotube-filled nanofiber yarns. *Adv. Mater.* **2003**, *15*, 1161–1165.

[16] Wang, J.; Dai, J.; Yarlagadda, T. Carbon nanotube-conducting-polymer composite nanowires. *Langmuir* **2005**, *21*, 9–12.

[17] Ribbe, A. E.; Bodycomb, J.; Hashimoto, T. Quantitative analysis of the staining of a polyisoprene-block-polystyrene. *Macromolecules* **1999**, *32*, 3154–3156.

[18] Rayson, M. J.; Briddon, P. R. Highly efficient method for Kohn–Sham density functional calculations of 500–10000 atom systems. *Phys. Rev. B* **2009**, *80*, 205104.

[19] Briddon, P. R.; Jones, R. LDA calculations using a basis of Gaussian orbitals. *Phys. Stat. Solidi B* **2000**, *217*, 131–171.

[20] Massuyeau, F.; Duvail, J. L.; Athalin, H.; Lorcy, J. M.; Lefrant, S.; Wéry, J.; Faulques, E. Elaboration of conjugated polymer nanowires and nanotubes for tunable photo-luminescence properties. *Nanotechnology* **2009**, *20*, 155701.

[21] Massuyeau, F.; Faulques, E.; Athalin, H.; Lefrant, S.; Duvail, J. L.; Wéry, J.; Mulazzi, E.; Perego, R. Steady state and transient photoluminescence in poly-p-phenylene vinylene films and nanofibers. *J. Chem. Phys.* **2009**, *130*, 124706.

[22] Stengersmith, J. D.; Lenz, R. W.; Wegner, G. Spectroscopic and cyclic voltammetric studies of poly(para-phenylene vinylene) prepared from 2 different sulfonium salt precursor polymers. *Polymer* **1989**, *30*, 1048–1053.

[23] Wéry, J.; Aarab, H.; Lefrant, S.; Faulques, E.; Mulazzi, E.; Perego, R. Photoexcitations in composites of poly(paraphenylene vinylene) and single-walled carbon nanotubes. *Phys. Rev. B* **2003**, *67*, 115202.

[24] Bachilo, S. M.; Strano, M. S.; Kittrell, C.; Hauge, R. H.; Smalley, R. E.; Weisman, R. B. Structure-assigned optical spectra of single-walled carbon nanotubes. *Science* **2002**, *298*, 2361–2366.

[25] Duesberg, G. S.; Loa, I.; Burghard, M.; Syassen, K.; Roth, S. Polarized Raman spectroscopy on isolated single-wall carbon nanotubes. *Phys. Rev. Lett.* **2000**, *85*, 5436–5439.

[26] Rao, A. M.; Jorio, A.; Pimenta, M. A.; Dantas, M. S. S.; Saito, R.; Dresselhaus, G.; Dresselhaus, M. S. Polarized Raman study of aligned multiwalled carbon nanotubes. *Phys. Rev. Lett.* **2000**, *84*, 1820–1823.

[27] Futaba, D. N.; Hata, K.; Yamada, T.; Hiraoka, T.; Hayamizu, Y.; Kakudate, Y.; Tanaike, O.; Hatori, H.; Yumura, M.;

Iijima, S. Shape-engineerable and highly densely packed single-walled carbon nanotubes and their application as super-capacitor electrodes. *Nat. Mater.* **2006**, *5*, 987–994.

[28] Lefebvre, J.; Fraser, J. M.; Finnie, P.; Homma, Y. Photoluminescence from an individual single-walled carbon nanotube. *Phys. Rev. B* **2004**, *69*, 075403.

[29] Liem, H. M.; Etchegoin, P.; Whitehead, K. S.; Bradley, D. D. C. Raman anisotropy measurements: An effective probe of molecular orientation in conjugated polymer thin films. *Adv. Funct. Mater.* **2003**, *13*, 66–72.

[30] Orion, I.; Buisson, J. P.; Lefrant, S. Spectroscopic studies of polaronic and bipolaronic species in n-doped poly(paraphenylenevinylene). *Phys. Rev. B* **1998**, *57*, 7050–7065.

[31] Mulazzi, E.; Perego, R.; Aarab, H.; Mihut, L.; Lefrant, S.; Faulques, E.; Wéry, J. Photoconductivity and optical properties in composites of poly(paraphenylene vinylene) and single-walled carbon nanotubes. *Phys. Rev. B* **2004**, *70*, 155206.

[32] Steinhart, M.; Wendorff, J. H.; Greiner, A.; Wehrspohn, R. B.; Nielsch, K.; Schilling, J.; Choi, J.; Gösele, U. Polymer nanotubes by wetting of ordered porous templates. *Science* **2002**, *296*, 1997.

[33] Hulteen, J. C.; Martin, C. R. A general template-based method for the preparation of nanomaterials. *J. Mater. Chem.* **1997**, *7*, 1075–1087.

[34] Panhuis, M. I. H.; Maiti, A.; Dalton, A. B.; van der Noort, A.; Coleman, J. N.; McCarthy, B.; Blau, W. J. Selective interaction in a polymer-single-wall carbon nanotube composite. *J. Phys. Chem. B* **2003**, *107*, 478–482.

[35] Chen, J.; Liu, H. Y.; Weimer, W. A.; Halls, M. D.; Waldeck, D. H.; Walker, G. C. Noncovalent engineering of carbon nanotube surfaces by rigid, functional conjugated polymers. *J. Am. Chem. Soc.* **2002**, *124*, 9034–9035.

[36] Kang, Y. K.; Lee, O. S.; Deria, P.; Kim, S. H.; Park, T. H.; Bonnell, D. A.; Saven, J. G.; Therien, M. J. Helical wrapping of single-walled carbon nanotubes by water soluble poly(p-phenyleneethynylene). *Nano Lett.* **2009**, *9*, 1414–1418.

[37] Gao, J.; Loi, M. A.; de Carvalho, E. J. F.; dos Santos, M. C. Selective wrapping and supramolecular structures of polyfluorene–carbon nanotube hybrids. *ACS Nano* **2011**, *5*, 3993–3999.

[38] Kymakis, E.; Amaratunga, G. A. J. Photovoltaic cells based on dye-sensitisation of single-wall carbon nanotubes in a polymer matrix. *Sol. Energ. Mat. Sol. C.* **2003**, *80*, 465–472.

[39] Kymakis, E.; Amaratunga, G. A. J. Single-wall carbon nanotube/conjugated polymer photovoltaic devices. *Appl. Phys. Lett.* **2002**, *80*, 112–114.

[40] Ltaief, A.; Bouazizi, A.; Davenas, J. Charge transport in carbon nanotubes–polymer composite photovoltaic cells. *Materials* **2009**, *2*, 710–718.

[41] Heun, S.; Mahrt, R. F.; Greiner, A.; Lemmer, U.; Bassler, H.; Halliday, D. A.; Bradley, D. D. C.; Burn, P. L.; Holmes, A. B. Conformational effects in poly(p-phenylene vinylene)s revealed by low-temperature site-selective fluorescence. *J. Phys.-Condens. Mat.* **1993**, *5*, 247–260.

[42] Holt, J. M.; Ferguson, A. J.; Kopidakis, N.; Larsen, B. A.; Bult, J.; Rumbles, G.; Blackburn, J. L. Prolonging charge separation in P3HT–SWNT composites using highly enriched semiconducting nanotubes. *Nano Lett.* **2010**, *10*, 4627–4633.